神戸大集中講義 2012 Part 2

担当 高薮縁 （東大大気海洋研究所）

「熱帯の気候形成： 対流」

- Mesoscale Convective Systems
  - レーダー観測
  - MCSの構造
  - MCSが環境場に与える効果

メソスケールシステムの観測

Synoptic Scale (総観規模)： ＞2000km

Mesoscale（メソスケール）： 2-2000km

メソαスケール 200-2000km

メソβスケール 20-200km

メソγスケール 2-20km

Convective Scale (対流スケール)：0.2-2km

Orlanski (1975)

Radar観測：対流スケールの分解能でメソスケールの広がりを捉えるのに適している。

レーダー観測

Radar Meteorology

'Mesoscale coverage and convective-scale resolution'

- range
  reflectivity
  velocity component
  + polarization

  Noncoherent/conventional radar

  Doppler radar (target veolcity)

  Polarimetric/multiple-polarization radar (target shape or orientation)

- 波長：1-30cm　短波長ほど感度は高いが減衰がきつい
  10cm(S-band)：降雨減衰が除ける最短波長
  ~8mのパラボラアンテナが必要
  5cm (C-band), 3cm (X-band): shipborne
  2cm(Ku-band): satellite borne : TRMM 13.6GHz
  1cm(Ka-band): satellite borne (solid phase): GPM 35.55GHz
  1-8mm : 雲レーダー
- スキャンタイム：2-10min
- 観測レンジ：200-400km, 定量的議論は100-200km

観測される値：時間平均(~0.01-0.1sec)パワー

$$\bar{P}_r = \frac{P_t G^2 \lambda^2 \theta_H \theta_V \tau_p c_o \eta_r}{512(2 \ln 2)\pi^2 r^2}$$

η_r : radar reflectivity per unit volume of air

rはレンジ

$$\eta_r = \sum \sigma$$

σ ：一つの粒子の有効後方散乱断面積

粒子直径 D < 0.1λなので、Rayleigh散乱理論が適用できる

$$\sigma = \pi^5 |K|^2 D^6 \lambda^{-4}$$

$|K|^2$は複素屈折率の関数で物質の特性に依存

liquid water: 0.92, ice: 0.197

レーダー反射因子：radar reflectivity factor Z : これが求められたら苦労しない

$$Z \equiv \frac{1}{\mathcal{V}_{\text{res}}} \sum D^6 = \frac{r^2 \bar{P}_r C_R}{|K|^2}$$

$$\mathcal{V}_{\text{res}} = \pi \theta_H \theta_V \left(\frac{r}{2}\right)^2 \frac{c_o \tau_p}{2}$$

$$C_R = \frac{64 \lambda^2 r^2}{P_t G^2 \pi^2 \mathcal{V}_{\text{res}}}$$

where P_t is the transmitted power, G is the antenna gain (a dimensionless number allowing for the focusing effect of the antenna), τ_p is the duration of the emitted radar pulse, c_o is the speed of light, θ_H and θ_V are the horizontal and vertical beamwidth angles (i.e., the angles between power points expressed in radians), respectively, and η_r is called the *radar reflectivity* per unit volume of air. It is the

実際には散乱粒子は様々な物質で構成される

： liquid, ice, melting ice, insects,…

→$|K|^2$ の値を確実に決める手段がない。

→ そこで通常、Z （レーダー反射因子）の代わりに

等価レーダー反射因子： equivalent radar reflectivity factor: Ze を用いる。

$$Z_e \equiv \frac{r^2 \bar{P}_r C_R}{0.93} \quad \text{mm}^6\,\text{m}^{-3}$$

注意：D^6で表現されるのはZであり、物理的にはZeはZに変換しなければ意味を持たない。Iceとわかっていれば、0.93/0.197を乗ずればよい。しかし、反射粒子の物質特性を完全に把握できないので、レーダーデータは通常Zeのまま用いる。

デシベル値で現すことが多い $\text{dB}Z_e \equiv 10 \log_{10} Z_e$

典型的には ~-30-0: marginally detectable
~0-10: drizzle, very light rain, light snow
~10-30: moderate rain, heavier snow
~30-45: melting snow
~30-60: moderate to heavy rain
~60-70 or more: hail

降水量推定法

4.2.2.1 Particle Size Method

the radar reflectivity factor $Z = \int_0^\infty D^6 N(D)\, dD$

the mixing ratio of rainfall, $q_r = \frac{\pi \rho_L}{6\rho} \int_0^\infty D^3 N(D)\, dD$

the rainfall rate $\Re = \frac{\pi \rho_L}{6} \int_0^\infty V(D) D^3 N(D)\, dD$

経験的にある限られた状況では

$Z = \tilde{a} \Re^{b}$

logZ vs. logR, logZ vs. logρq_rは線形関係にあるから

$Z = \tilde{a}_1 (\rho q_r)^{\tilde{b}_1}$

$\Re/(\rho q_r) = \hat{V} \equiv \frac{\int_0^\infty V(D) \mathrm{m}(D) N(D)\, dD}{\int_0^\infty \mathrm{m}(D) N(D)\, dD}$ the mass-weighted fall velocity

$\hat{V} = \tilde{a}_2 Z^{\tilde{b}_2}$ → しかし結局ZeをZに変換しなければならず、不確実性が大きい。

特徴的なレーダーエコー

地上に落ちるまでに1-3時間：雨滴の成長に時間がある。deposition: 沈着, aggregation: 凝集

層状雨

Stratiform rain

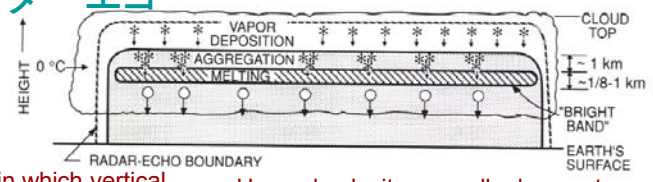

Precipitation process in which vertical motion is small compared to the fall veolcity of ice crystals and snow

Upward velocity normally does not exceed a few tens of cms per second

$|w| < V_{ice}$ $V_{ice} \sim 1 - 3 ms^{-1}$

対流雨

Convective rain

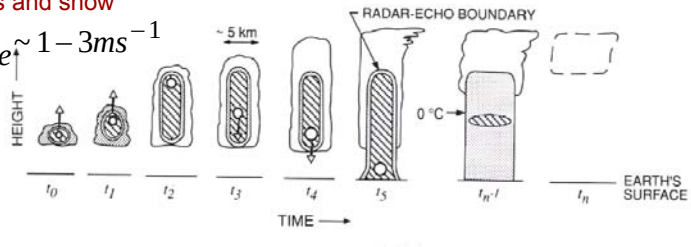

W ~ 1-10m/s > Vice

Often rain reaches the ground within ½ hours of cloud formation

Accretion of liq. Water

衝突併合

Figure 6.1 (a) Characteristics of stratiform precipitation. (b) Characteristics of convective precipitation. Shading shows higher intensities of radar echo, with hatching indicating the strongest echo. In (b) cloud is shown at a succession of times $t_0, \ldots, t_n$. Growing precipitation particle is carried upward by strong updrafts until t_2 and then falls relative to the ground, reaching the surface just after t_5. After t_5, the cloud may die or continue for a considerable time in a steady state before dissipation sets in at t_{n-1} and t_n. The dashed boundary indicates an evaporating cloud. (From Houze, 1981. © American Geophysical Union.)

Bright Band

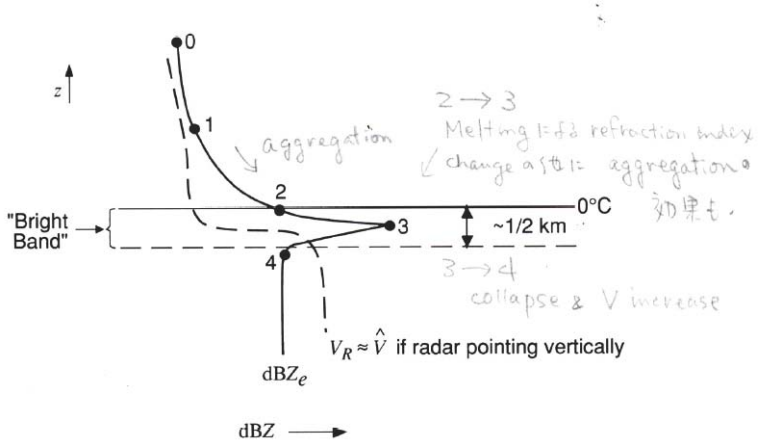

Figure 6.2 Schematic of vertical profile of radar data in stratiform precipitation. Solid curve ows reflectivity. Dashed curve shows Doppler radial velocity V_R with the antenna at vertical cidence. Under stratiform conditions V_R is related approximately to the mass-weighted terminal fall eed of the particles, $\hat{V}$. Layers in which different microphysical processes dominate are bounded by ints 0–4 (see text for further discussion).

雲クラスター

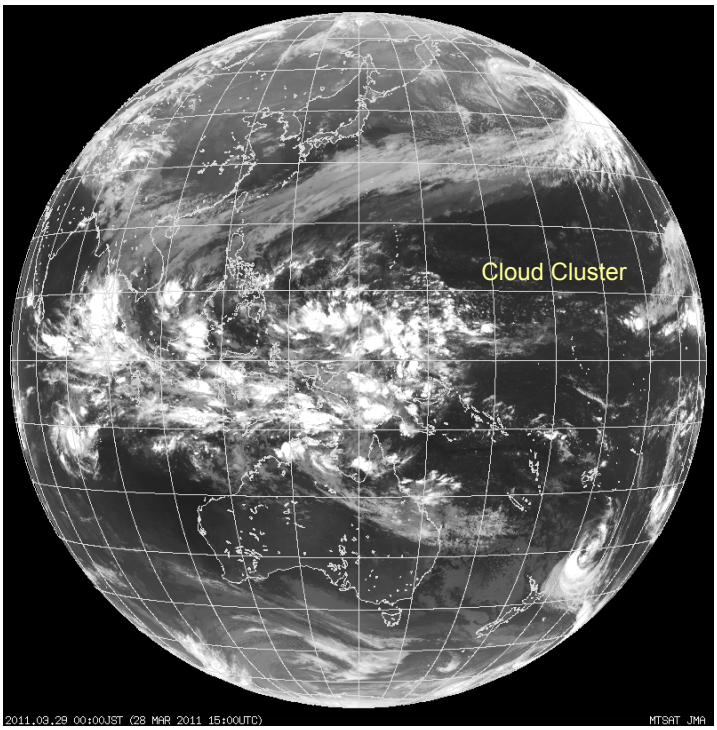

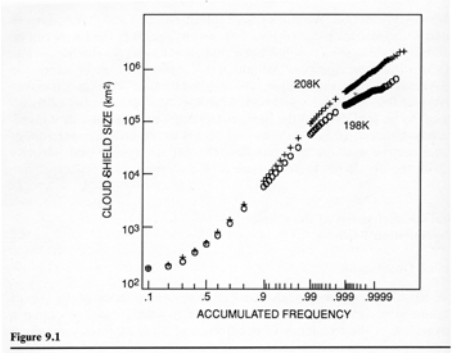

Figure 9.1

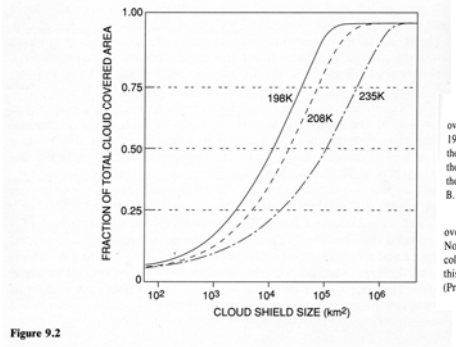

Figure 9.2

Accumulated Frequency Distribution (IR)

208Kの閾値で50,000km²を超えるシステムは数で1%だが、総雲域の40%を占める。雲と降水との関係から総降雨量に対する貢献も40%程度と見積もられる。

For cloud clusters defined with 208K threshold, ones with area > 50,000km² account for only 1% in numbers, but for 40% in total cloud area. Statistical relation suggests that these gigantic systems also account for 40% in precipitation amount.

Figure 9.1 Spectrum of sizes of the cloud shields seen in geostationary satellite infrared imagery over the tropical region bounded by 70°E, 170°W, 25°N, and 25°S during November–February of 1986–1987, 1987–1988, and 1988–1989. The plot is in log-probability format, which means that the ordinate scale is labled such that if the log of the quantity represented is normally distributed, the curve of the accumulated frequency distribution will be a straight line. The cloud shields for the two curves are defined by infrared temperature thresholds of 198 K and 208 K. (Provided by B. E. Mapes.)

Figure 9.2 Areal coverage by the cloud shields seen in geostationary satellite infrared imagery over the region of the western tropical Pacific (bounded by 70°E and 170°W, 25°N, and 25°S) during November–February of 1986–1987, 1987–1988, and 1988–1989. The total area covered by clouds colder than the indicated threshold temperature has been determined. The plot shows the fraction of this total area accounted for by cloud shields up to the size indicated on the ordinate of the plot. (Provided by B. E. Mapes.)

MCSの構造

熱帯海上の雲クラスターの概念図

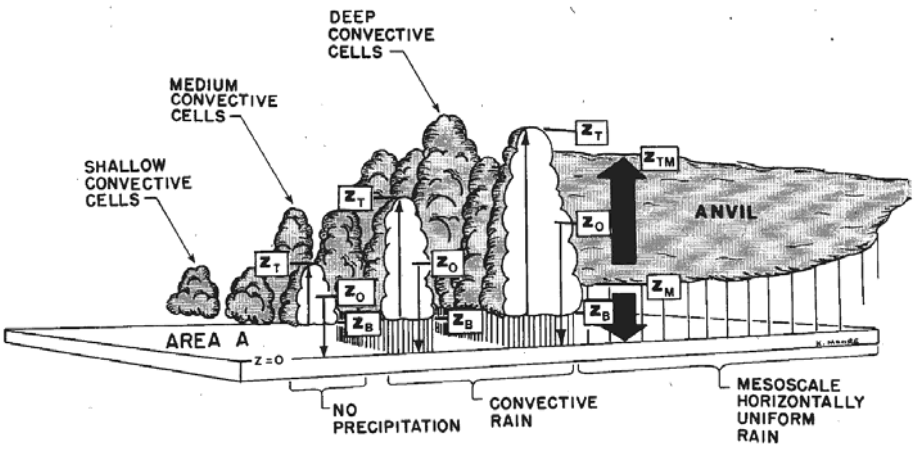

FIG. 1. Schematic of a typical population of clouds over a tropical ocean. Thin arrows represent convective-scale updrafts and downdrafts. Wide arrows represent mesoscale updrafts and downdrafts. Other details and symbols are described in the text.

MCSの特徴的な構造 (レーダー)

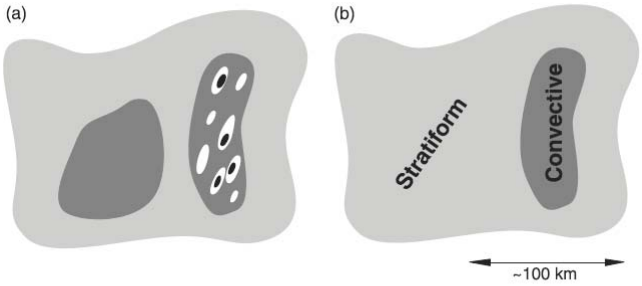

Figure 2. (a) Idealization of a horizontal map of radar reflectivity (b) divided into convective and stratiform regions. From *Houze* [1997].

対流雨域：強く鉛直に伸びたコアで形成されている。
層状雨域：比較的一様で弱い雨、一部は衰退した古い対流セルから、一部は広く傾いたメソスケールの層状の上昇によって形成されている。

Precipitation structure of a squall line sysytem GATE

スコールラインシステムの降雨構造

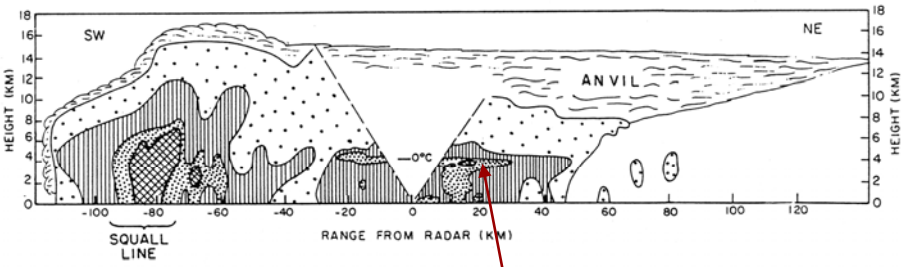

FIG. 25. RHI through entire squall-line system, along azimuths 223° (SW) and 43° (NE) from *Oceanographer* radar at 1545 GMT 4 September 1974 (see Fig. 17j). Inside contours are for 38, 33, 23 dBZ and minimum detectable echo. Outside scalloped contour outlines cloud boundary estimated from infrared satellite imagery.

Bright band

(Houze 1977)

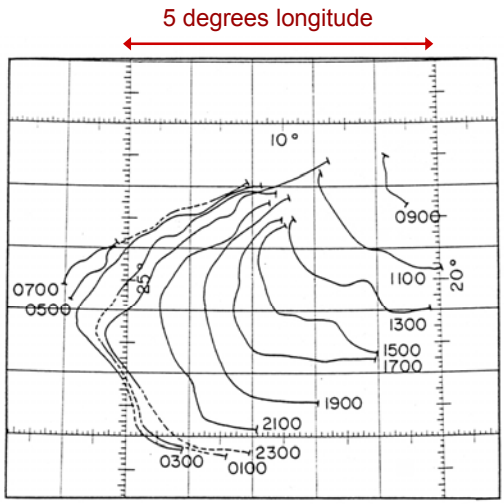

FIG. 16. Successive positions of the leading edge of the squall line. Times are GMT, beginning with 0900 on 4 September and ending with 0700 on 5 September 1974.

Squall line のleading edge

Propagation spd: ~50km/hr

(Houze 1977)

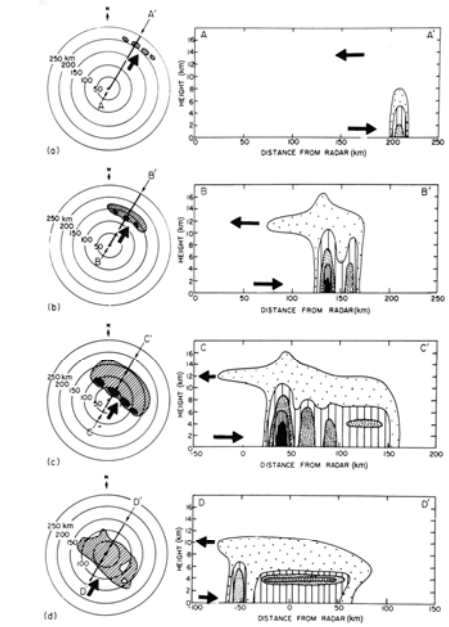

Figure 9.11 Schematic of the life cycle of the precipitation area of a mesoscale convective system as it would appear on radar in horizontal and vertical cross sections during (a) formative, (b) intensifying, (c) mature, and (d) dissipating stages. The outside contour of radar reflectivity represents the weakest detectable echo. The inner contours are for successively higher reflectivity values. Heavy arrows indicate the direction of the wind relative to the system. (From Leary and Houze, 1979a. Reproduced with permission from the American Meteorological Society.)

Radar

MCSの降雨域のライフサイクル

Schematic of the life cycle of the precipitation of a mesoscale convective system

(Leary and Houze 1979)

最初の数時間は対流が繰り返し立つがまだ組織化されない。降水に伴う下層の冷気プールが強まると、傾いたメソスケールの循環が発達しスコールラインシステムが出来上がってくる。

前方に新しい対流雲群が形成され、最初の対流雲群の残骸が厚い乱層雲となる→anvil shield

Mature stage: 5-10hr

Radar & IR

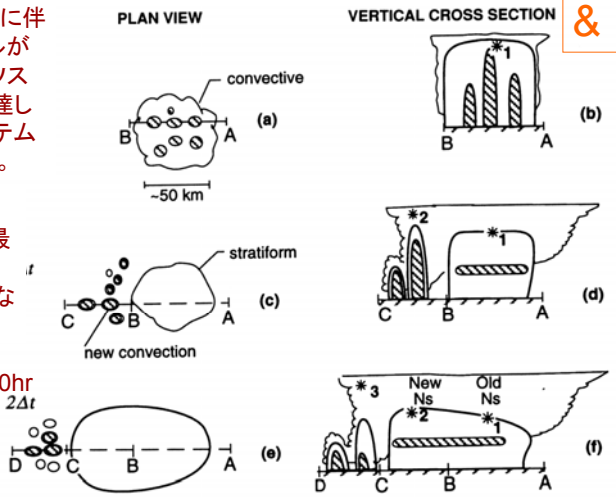

Figure 6.11 Conceptual model of the development of nimbostratus associated with deep convection. Panels (a), (c), and (e) show horizontal radar echo pattern at the earth's surface with two levels of intensity at three times, t_o, $t_o + \Delta t$, and $t_o + 2\Delta t$. Panels (b), (d), and (f) show corresponding vertical cross sections. A sketch of the visible cloud boundary has been added to the vertical cross sections. Asterisks trace the fallout of three ice particles.

(Leary and Houze 1979)

Schematic

GATE squall line

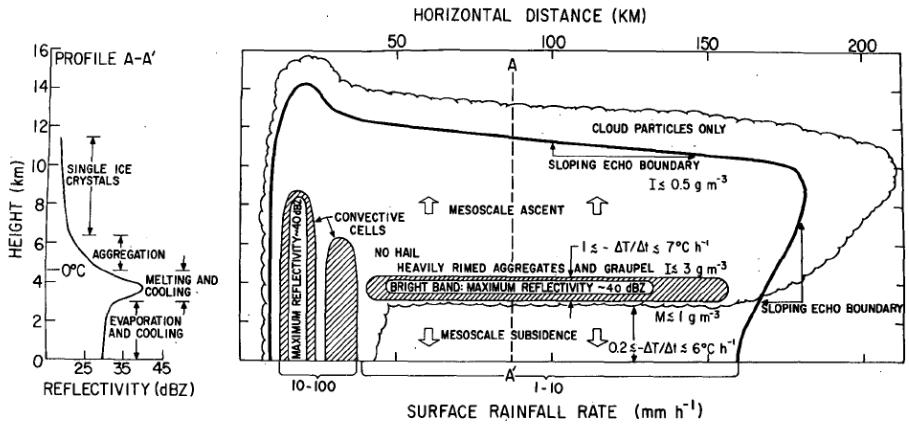

FIG. 8. Schematic vertical cross section and vertical profile of radar reflectivity (along dashed line A–A′ in the cross section) in horizontally uniform precipitation associated with an anvil cloud. The anvil cloud occurs to the rear of intense convective cells propagating in the direction from right to left in the figure. The dark solid line is the contour of minimum detectable radar echo, lighter solid lines and shading indicate contours of higher reflectivity, and the scalloped line indicates the cloud boundary.

Leary and Houze 1979b

MCSの降雨機構

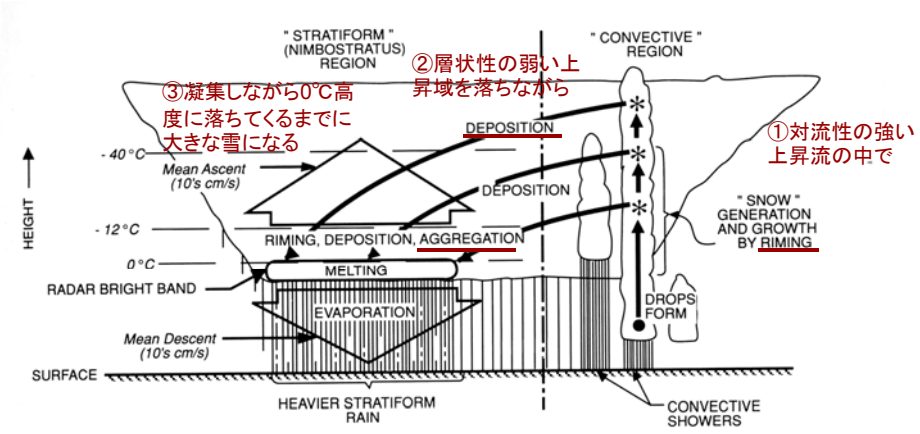

Figure 6.12 Schematic of the precipitation mechanisms in a mesoscale convective system. Solid arrows indicate particle trajectories. (From Houze, 1989. Reprinted with permission from the Royal Meteorological Society.)

Deposition: 昇華凝結：氷晶核上への水蒸気の昇華凝結

Riming :着氷： 衝突した過冷却雲粒が凍結して雪片を成長させる

Aggregation: 凝集： 氷粒子が別の氷粒子を集めて成長する (Houze 1989)

MCSの鉛直流とレーダー反射因子コンポジット構造

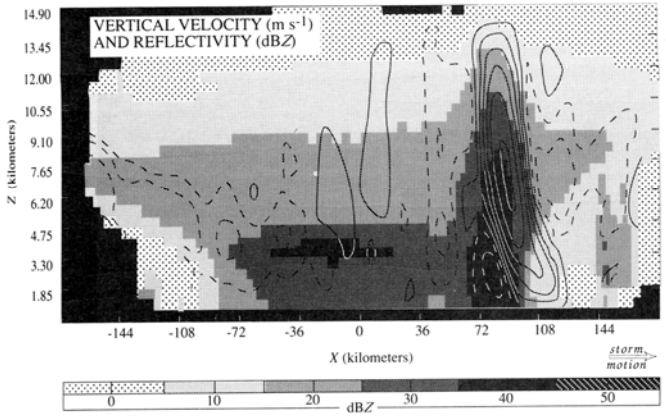

Doppler radar による鉛直風とレーダー反射因子の観測

Figure 9.31 Composite radar reflectivity and vertical velocity fields constructed from Doppler radar observations obtained at different locations and times within a squall line with trailing stratiform precipitation. Other aspects of this storm are illustrated in Figs. 9.15, 9.18, 9.34, 9.40, 9.41, 9.43, 9.44, 9.45, 9.48, 9.53, and 9.54. All the data in a 60-km-wide strip oriented perpendicular to the convective line and extending across the system were combined, averaged, and filtered to obtain the mean cross section. X is the coordinate axis perpendicular to the line. The storm was moving from left to right. Radar reflectivity (dBZ) is shown by shading. Vertical wind component is shown by contours for −0.9, −0.45, −0.15, 0.15, 0.45, 0.9, 1.5, 2.4, and 3.6 m s^{-1} with negative values dashed. (From Biggerstaff and Houze, 1993. Reproduced with permission from the American Meteorological Society.)

(Biggerstaff and Houze 1993)

Dual Dopplerレーダー観測
1985年6月11日Kansas squall line

上昇流のピークは後方に向かって徐々に高度が上がる。対流域の強いダウンドラフトセルも観測される。

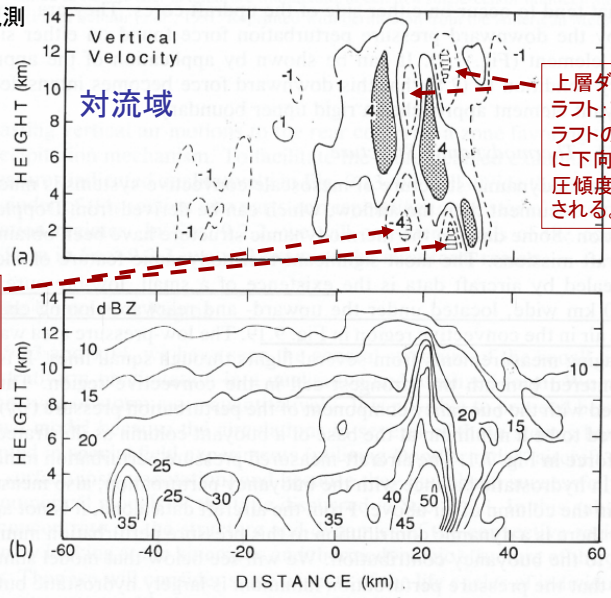

上層ダウンドラフト：アップドラフトの両側に下向きの気圧傾度で生成される。

下層ダウンドラフト：激しい降水に伴って生成される。Cold pool を形成する。

Figure 9.18 Isotachs of (a) vertical velocity (m s^{-1}) and (b) radar reflectivity (dBZ) in the convective region of a squall line with trailing stratiform precipitation. Other aspects of this storm are illustrated in Figs. 9.15, 9.31, 9.34, 9.40, 9.41, 9.43, 9.44, 9.45, 9.48, 9.53, and 9.54. (From Houze, 1989. Reprinted with permission from the Royal Meteorological Society.)

(Houze 1989)

Gust Front

$$\frac{Du}{Dt} = -\frac{1}{\rho_o}\frac{\partial p^*}{\partial x}$$

p*は周囲の静水圧平衡からのずれ

Gust frontと共に動く座標系、定常を仮定

$$\frac{\partial(u^2/2)}{\partial x} = -\frac{1}{\rho_o}\frac{\partial p^*}{\partial x}$$

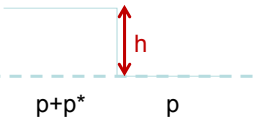

重力流の深さh、密度$\rho_0+\Delta\rho$

$$\frac{U_f^2}{2} = g\frac{\Delta\rho}{\rho_o}h$$

p* =ghΔρ

重力流のスピード：密度差と深さで決まる

(Houze, 1993)

水の蒸発を伴うダウンドラフト
→cold pool を生成

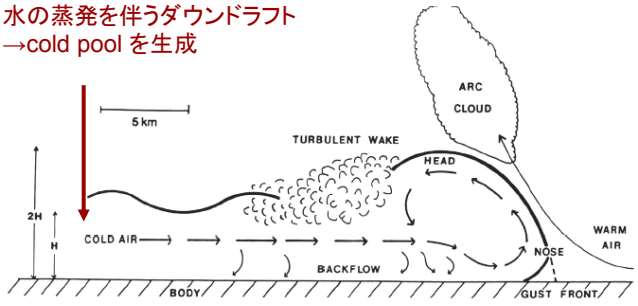

Figure 8.39 Schematic cross section through the gust front of a thunderstorm. (From Droegemeier and Wilhelmson, 1987; based on earlier studies of Charba, 1974; Goff, 1975; Wakimoto, 1982; Koch, 1984. Reprinted with permission from the American Meteorological Society.)

メソスケールの高低気圧構造

融解層の上下に生じるメソスケールに広がったhighとlow

対流加熱の下
Hydrostatic low

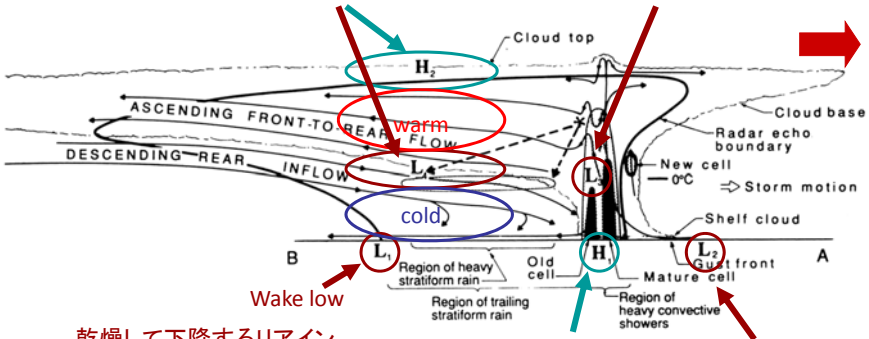

Wake low

乾燥して下降するリアインフローによる気温上昇

→層状雨域のすぐ後方にsfc lowを生じる。

Hydrostatic gust front high

中上層の補償下降流によって生成されるsurface low

Radar & Air Craft

(Houze et al. 1989)

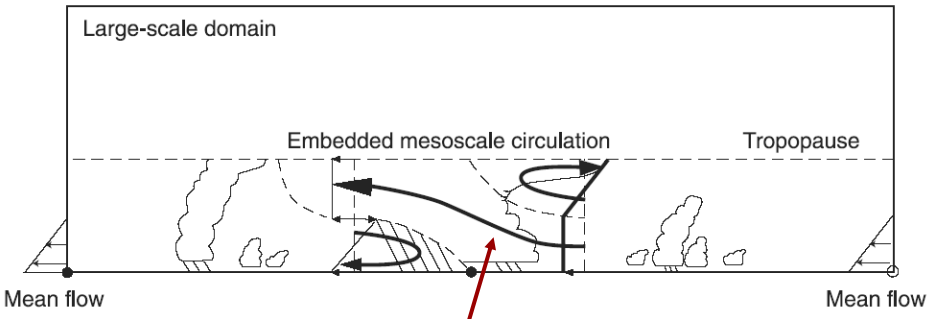

Figure 6. Schematic diagram showing the airflow relative to a two-dimensional, steady state mesoscale convective system in a large-scale environment of given wind shear. The environmental air entering the updraft is potentially unstable, and there is a pressure decrease across the system from right to left at middle levels. The streamlines are those required by conservation of mass, momentum, entropy, and vorticity. Adapted from *Moncrieff* [1992].

中層での、図右から左への気圧降下が、層として傾斜して持ち上がる空気の流れを維持している。

(Moncrieff 1992)

MCSの相対的な流れ

リアインフローの上方の斜め上向きの流れは、対流から降る氷粒子を後方に運ぶ

強い上昇流とその後方中上層のダウンドラフト

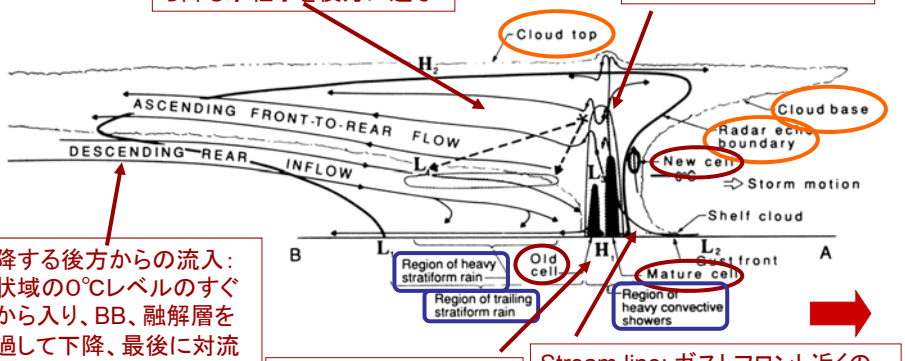

下降する後方からの流入：層状域の0℃レベルのすぐ上から入り、BB、融解層を通過して下降、最後に対流域の後方下層に入り込み対流を促進する。流入の強さはケースにより異なる。

Radar & Air Craft

Mature~old cells の強雨の中では、下層の対流スケールのダウンドラフトがガストフロントの後方からシステムの後方に向かって境界層内を広がる。

Stream line: ガストフロント近くの境界層から出発し、対流域を通過して後方の層状域の中上層にゆっくり上昇しながら入っていく

(Houze et al. 1989)

Air Craft

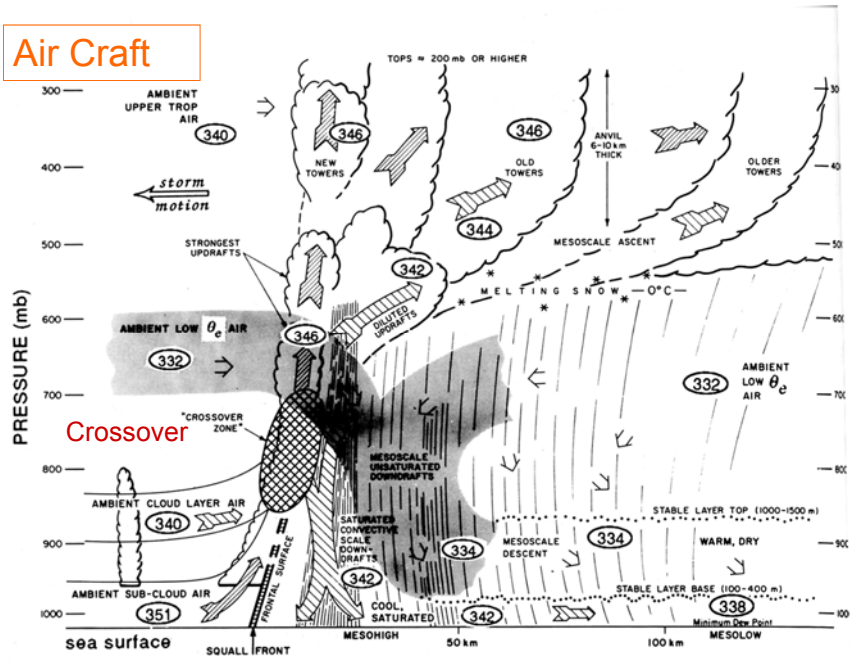

(Zipser 1977)

Zipser, Meitin, and LeMone, 1981

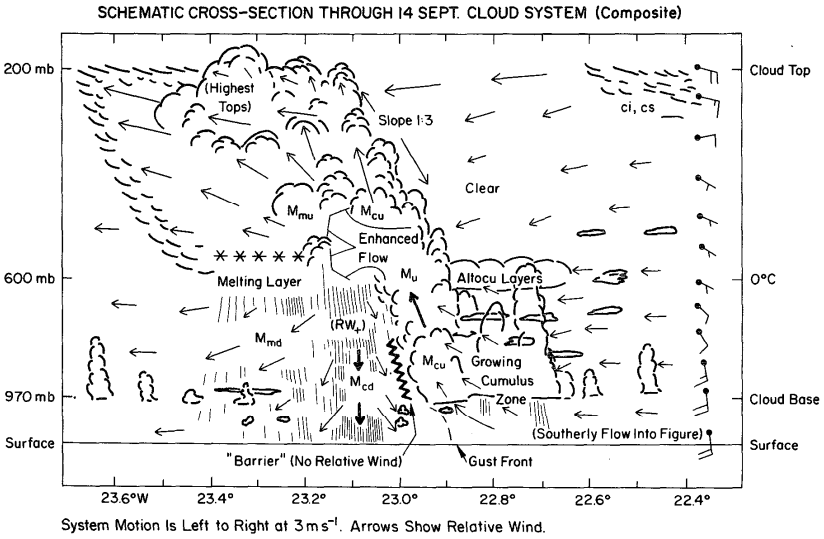

FIG. 8. Cross section through the north–south convective band constructed as a composite, representing best the time period of leg 5 (~1333 GMT). System motion is left to right at 2.5 m s⁻¹. The wind arrows along the right margin represent the large-scale flow field; each full barb is 5 m s⁻¹. The small arrows throughout the system represent flow relative to the system in the normal and vertical directions, based on Figs. 3 and 4 but partially schematic. See text.

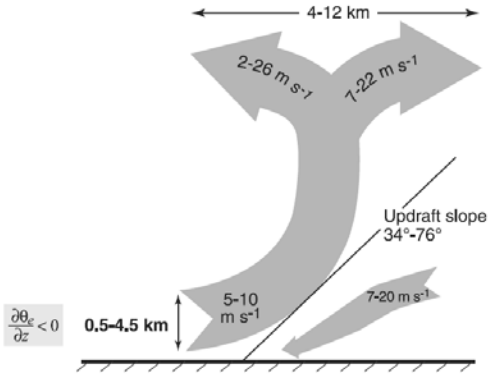

Figure 9. Schematic of airflow in the convective regions of an MCS over the western tropical Pacific as observed by airborne Doppler radar in Tropical Ocean–Global Atmosphere Coupled Ocean-Atmosphere Response Experiment (TOGA COARE). The numbers (from bottom to top) indicate the observed ranges of values of the depth of the inflow layer, horizontal relative velocity of inflow and outflow air currents, the slope of the updraft (angle measured relative to the ocean surface), and the width of the divergent region aloft. The horizontal directional differences of the low level updraft inflow and middle level downdraft inflow were often significantly different from 180°. Based on figures and tables from *Kingsmill and Houze* [1999a].

Airborne Doppler Radar

TOGA COARE

33 dual-Doppler Radar analyses from 25 different MCS + countless single Doppler sweeps from vertically scanning Doppler radars

- 上昇域はほとんど必ず傾斜した層状の上昇であり、明らかにダウンドラフトから形成されたcold poolの上に乗り上げる流れであった。
- 傾斜した上昇流の層の厚さは、0.5-4.5kmの範囲であり、大気境界層より明白に厚かった。

(Kingsmill and Houze 1999)

マルチセルストーム（Browning et al. 1976）

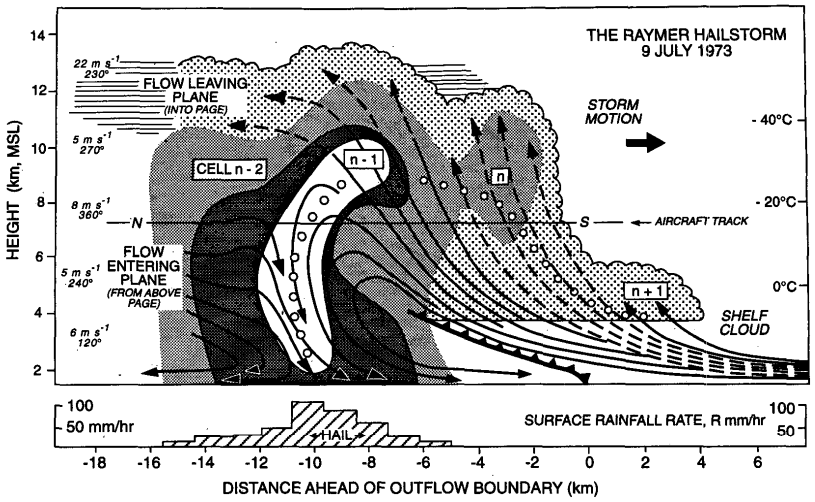

FIG. 1. Schematic model of a multicell storm in northern Colorado showing a vertical section along its direction of motion. Thick lines are smoothed streamlines of flow relative to the moving storm; they are broken on the left side of the figure to represent flow into and out of the plane and on the right side of the figure to represent flow remaining within a plane a few kilometers closer to the reader. Lightly stippled shading: extent of cloud; darker grades of shading: radar reflectivities of 35, 45, and 50 dBZ; open circles: trajectory of a hailstone during its growth from a small particle. Right: temperature scale; temperature of a parcel lifted from the surface. Left: environmental winds relative to the storm based on soundings behind the storm. Surface rainfall rates averaged over 2-min intervals during the passage of the storm are plotted at the bottom of the figure (from Browning et al. 1976).

Yang and Houze (1995a)

マルチセルMCSの重力波構造の概念図 （モデル）

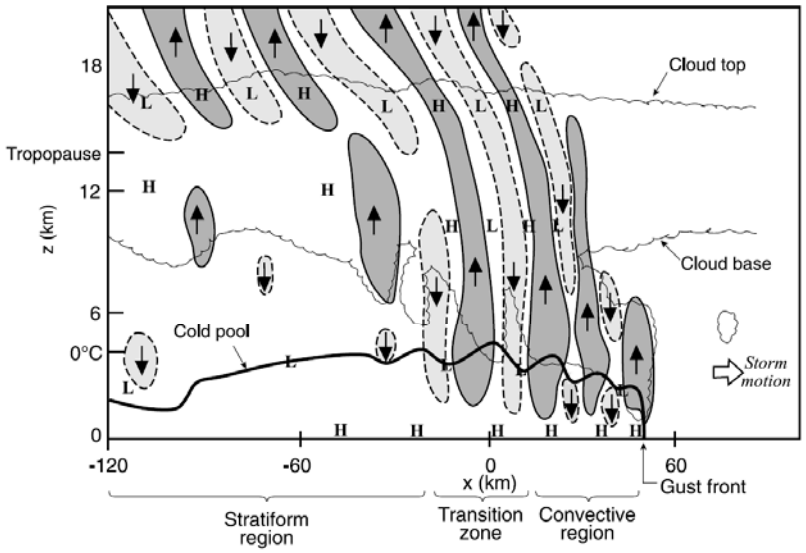

Figure 16. Schematic model of the gravity wave structure of a simulated multicellular MCS at a mature stage of development. Updrafts >1 m s^{-1} are heavily shaded. Downdrafts <−1 m s^{-1} are lightly shaded. Bold line is the cold pool outline defined by the −1 K potential temperature perturbation. Cloud outline is for the 0.5 g kg^{-1} contour of nonprecipitating hydrometeor mixing ratio. L and H indicate centers of low and high perturbation pressure, respectively. From *Yang and Houze* [1995a].

Yang and Houze (1995a)

スコールラインの環境場と層状域の大気成層構造

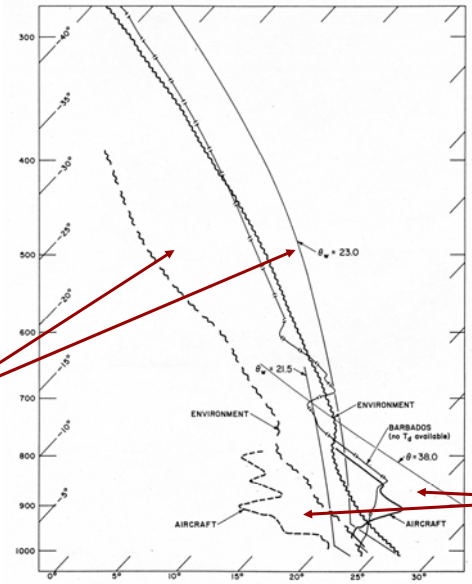

Squall line
の環境場

層状域の
観測

FIG. 5. Soundings pertaining to the 18 August 1968 squall line. The aircraft sounding is behind the squall along the climb shown in the Fig. 3 cross section. The Barbados sounding is also post-squall, at 1400 AST. The environment sounding is a composite of three pre-squall soundings, also from Barbados.

(Zipser 1977)

スコールライン通過後に特徴的な大気成層構造

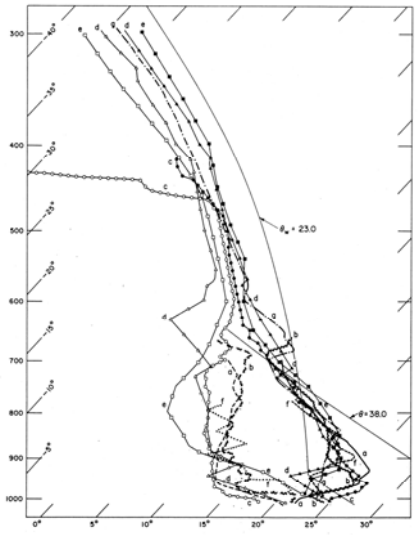

Characteristic
soundings in post
squall regions

FIG. 8. Characteristic soundings in post-squall regions. (a) 5 September 1974 by NCAR Queen Air, mostly in rain; (b) 1630 GMT, 12 September 1974, from the *Fay* (GATE position 28A, about 200 km behind leading edge and 50 km behind trailing precipitation); (c) 1804 GMT 12 September 1974, from the *Oceanographer* (GATE position 4, about 250 km behind leading edge and 100 km behind trailing precipitation); (d) 1130 GMT 12 September 1974, from the *Forye* (GATE position 10, about 350 km behind leading edge and 174 km behind trailing precipitation); (e) 2000 AST 28 August 1969, Anaco, Venezuela, about 50 km behind trailing precipitation; (f) aircraft sounding from Fig. 6; (g) Barbados sounding from Fig. 6 (no T_d available).

(Zipser 1977)

Radiosonde

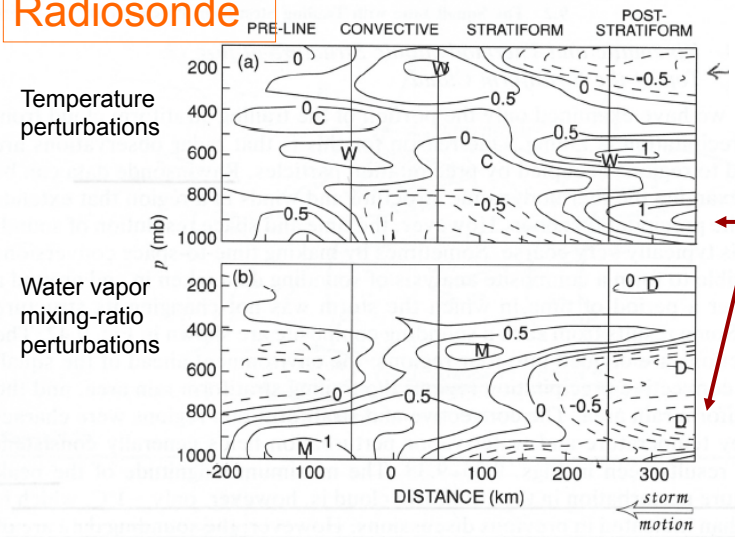

Figure 9.42 Composite analysis of radiosonde data obtained in and around a tropical squall-line system over the eastern Atlantic Ocean. Cross sections are along a line perpendicular to the leading convective region. (a) Temperature perturbation (K); maxima indicated by W, minima by C. (b) Water vapor mixing ratio perturbation (g kg^{-1}); maxima indicated by M, minima by D. Other aspects of this storm are illustrated in Figs. 9.50 and 9.59. (From Gamache and Houze, 1985. Reproduced with permission from the American Meteorological Society.)

Wake Low

乾燥して下降するリアインフローによる気温上昇

→層状雨域のすぐ後方にsfc lowを生じる。

Strong adiabatic warming associated with the subsiding rear inflow is found immediately to the rear of the strat. precip.

→ strong positive-temperature maximum at low levels

Schematic

Wake Low

Johnson and Hamilton, 1988

Oklahoma-Kansas PRESTORM experiment

arrows

(a) system relative sfc winds

(b) Ground relative sfc winds

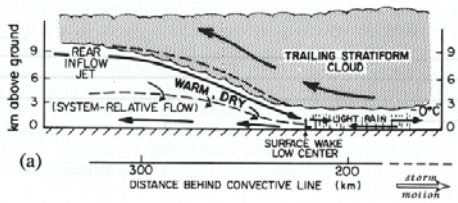

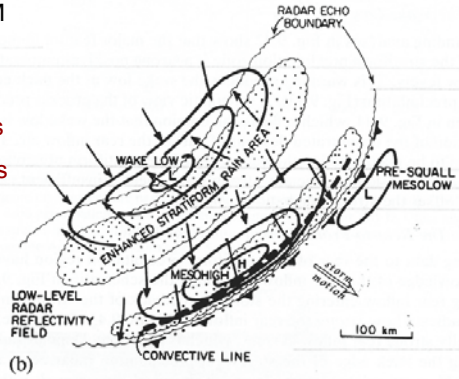

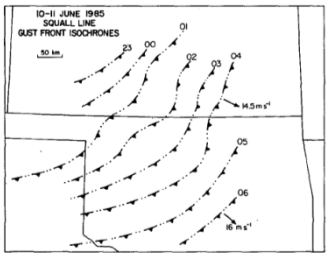

FIG. 4. Squall-line gust front isochrones for 10–11 June 1985, determined from surface mesonetwork data. Extensions outside mesonetwork area are estimated from radar data.

Figure 9.44 Schematic view of the process producing the wake low at the rear of a squall line with trailing stratiform precipitation. (a) Vertical cross section through wake low. (b) Plan view of surface winds and precipitation. Winds in (a) are system relative, with dashed line denoting zero relative wind. Arrows indicate streamlines, not trajectories, with those in (b) representing ground-relative wind. Note that horizontal scales are different in the two schematics. Other aspects of this storm are illustrated in Figs. 9.15, 9.18, 9.31, 9.34, 9.40, 9.41, 9.43, 9.45, 9.48, 9.53, and 9.54. (From Johnson and Hamilton, 1988. Reprinted with permission from the American Meteorological Society.)

Mesoscale Convective Vortex (MCV)

MCSに伴う中層渦

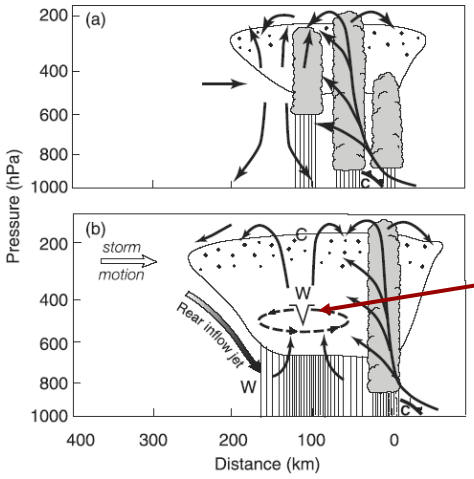

実際には、リアインフローはMCVに回り込んで行くものもある。

Figure 21. Schematic diagrams of the structure of an MCS with the leading convective line (shading) and the trailing-stratiform rain region (outlined) and the associated meso-vortex at (a) initial stage and (b) mesovortex genesis stage. The solid arrows represent the mesoscale circulation. The shaded arrow indicates the location of a rear inflow. W and C mark the regions of positive and negative temperature anomalies, respectively; V and dashed-line arrows denote a middle level mesoscale vortex. From *Chen and Frank* [1993].

MCV and rear inflow

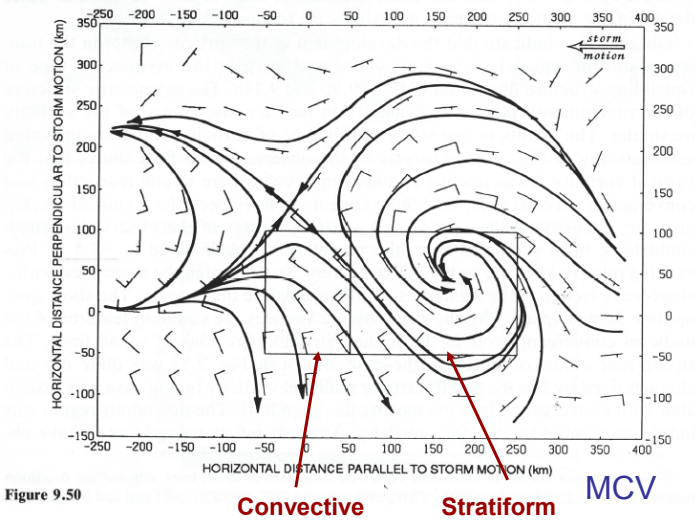

Figure 9.50

Mesoscale bandpass filtered 650hPa winds

（注意）

層状域は定量的にもほぼよいが、対流域の現象はこのBPFでは抽出できない。

MCV

Convective region of the squall line

Stratiform region

(Gamache and Houze 1985)

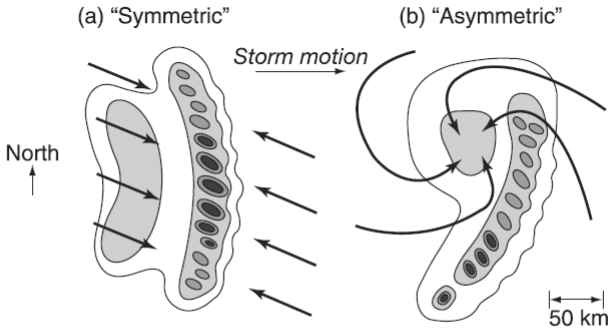

Figure 23. (a) Symmetric and (b) asymmetric paradigms of leading-line/trailing-stratiform squall line MCS structure in the Northern Hemisphere. Contour thresholds indicate radar reflectivity of increasing intensity. Convective regions have cores of maximum reflectivity (dark shading). Stratiform regions are centered on the areas of medium intensity echo (light shading) with no maximum reflectivity cores. Streamlines indicate low level wind direction. Adapted from *Houze et al.* [1989, 1990].

リアインフローは、対称的なシステム(a)の風の変化に伴うものの場合と非対称なシステム（b）の中層のメソスケール渦の一部である場合とがある。

(Houze et al. 1989,1990)

MCVが残る

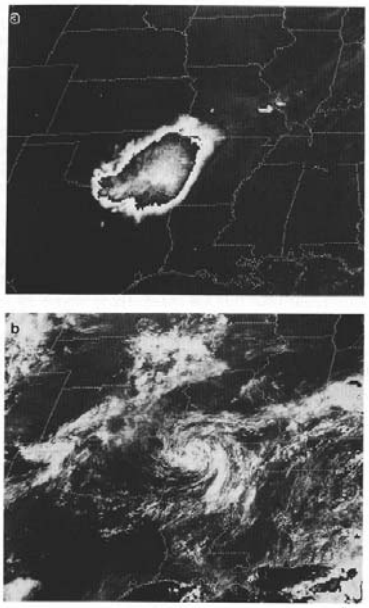

MCVが残る

Figure 9.63 (a) Infrared satellite view of a mesoscale convective complex (MCC) centered over Oklahoma at 1131 GMT 7 July 1982. Gray shades are proportional to infrared radiative temperature at cloud top, with coldest values indicated by light shading in the interior of the cloud system. The large cold cloud shield marks the MCC. (b) Visible satellite image of the remnants of the same MCC at 1631 GMT. A cyclonic circulation is seen in the cloud pattern over northwestern Arkansas. (Photos provided by J.M. Fritsch.)

環境場に与える効果
1．潜熱加熱

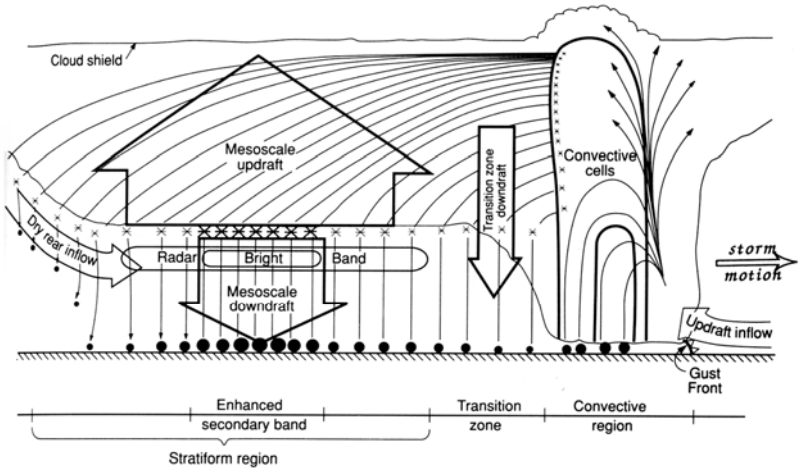

Figure 9.34 Schematic of the two-dimensional hydrometeor trajectories through the stratiform region of a squall line with trailing stratiform precipitation. Trajectories were based on fall speeds and air motions measured by Doppler radar. Other aspects of this storm are illustrated in Figs. 9.15, 9.18, 9.31, 9.40, 9.41, 9.43, 9.44, 9.45, 9.48, 9.53, and 9.54. (From Biggerstaff and Houze, 1991a. Reproduced with permission from the American Meteorological Society.)

(Biggerstaff and Houze 1991a)

MCSに伴う潜熱加熱

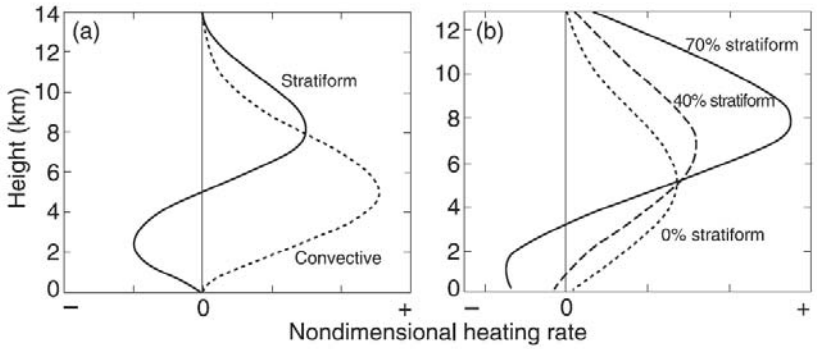

Figure 4. (a) Idealized profiles of net heating associated with convective and stratiform precipitation in a mesoscale convective system. The *x* axis is nondimensional until precipitation amounts are specified for the convective and stratiform regions. (b) Profiles of net heating by a mesoscale convective system with different fractions of stratiform precipitation. Adapted from *Schumacher et al.* [2004].

(Schumacher et al. 2004)

Radar

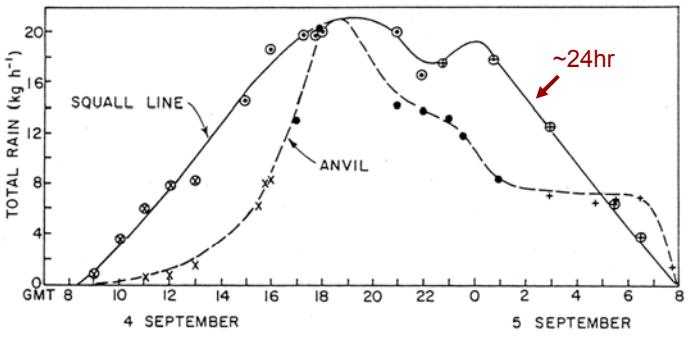

FIG. 26. Total rain integrated over areas covered by squall line and anvil portions of the squall-line system. Circled points refer to squall line region. Data points derived from *Oceanographer* radar echo patterns are indicated by ×'s. Points derived from composite *Oceanographer* and *Researcher* radar echo patterns indicated by dots. Points derived from composite *Oceanographer*, *Researcher* and *Gilliss* echo patterns are indicated by crosses.

Typically, stratiform rain contributes 20-50% to the total precipitation in the total life cycle of MCS. (Houze 1977)

In this case, the stratiform rain accounted for about 40%

Simulation

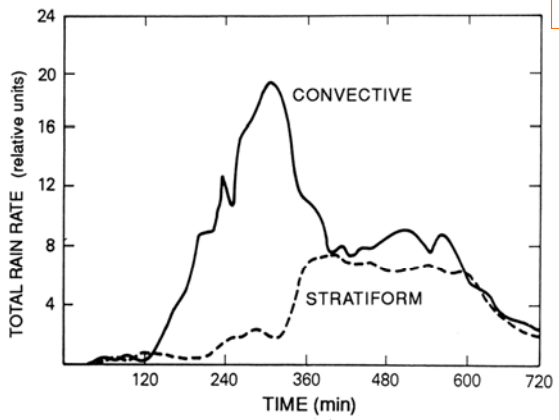

Figure 9.32 Area-integrated rain rate in a two-dimensional numerical-model simulation of a squall line with trailing stratiform region with ice-phase microphysics included. Rain amounts are summed separately for rain falling at grid points designated as convective and stratiform for each time step throughout the lifetime of the storm. (From Tao and Simpson, 1989. Reprinted with permission from the American Meteorological Society.)

シミュレートされたスコールラインは時空間ともにサイズがやや小さいが感じはよく出ている。

Stratiform rain ~37%

(Tao and Simpson 1989)

Stratiform Rain Ratio

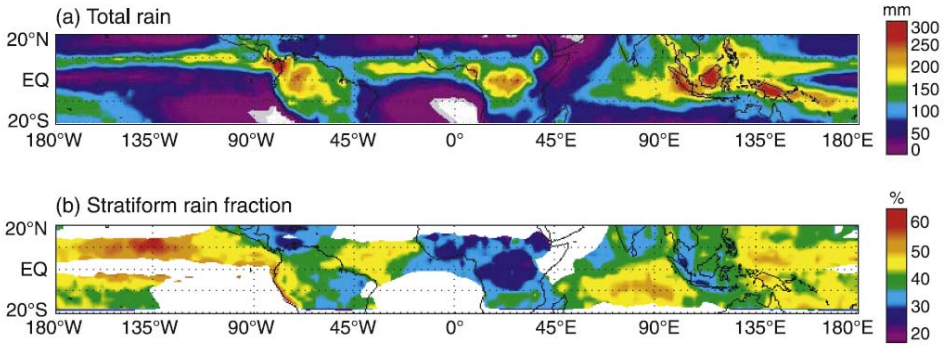

Figure 49. (a) Annual rainfall and (b) fraction of the annual rainfall that is stratiform, as determined from the TRMM PR by methods described by *Schumacher and Houze* [2003]. Courtesy of C. Schumacher.

(Schumacher and Houze, 2003)

TRMM SLH Q1-QR ALL 98-07
20N-20S

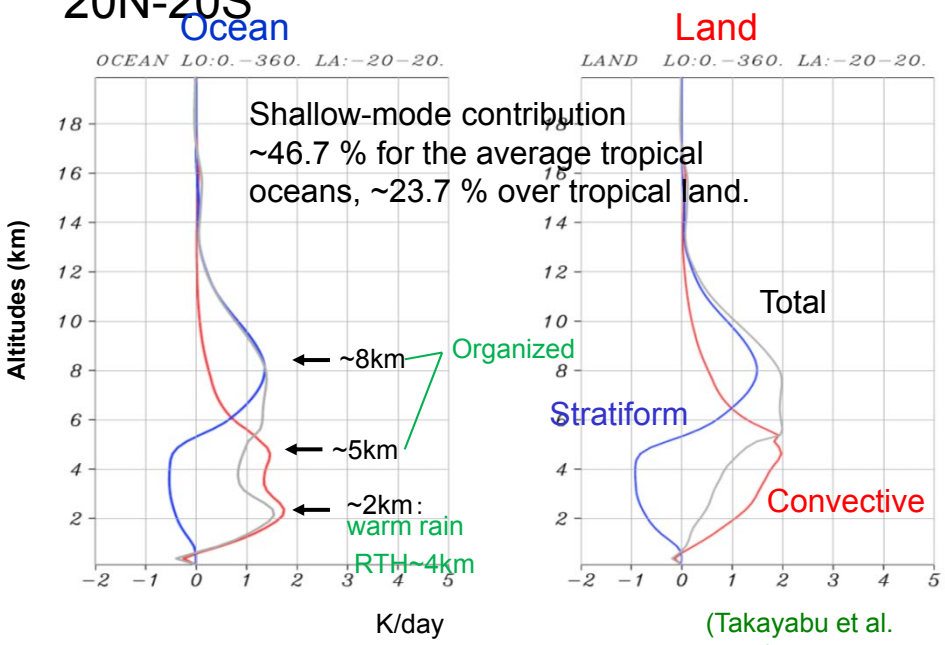

Responses to deep and shallow

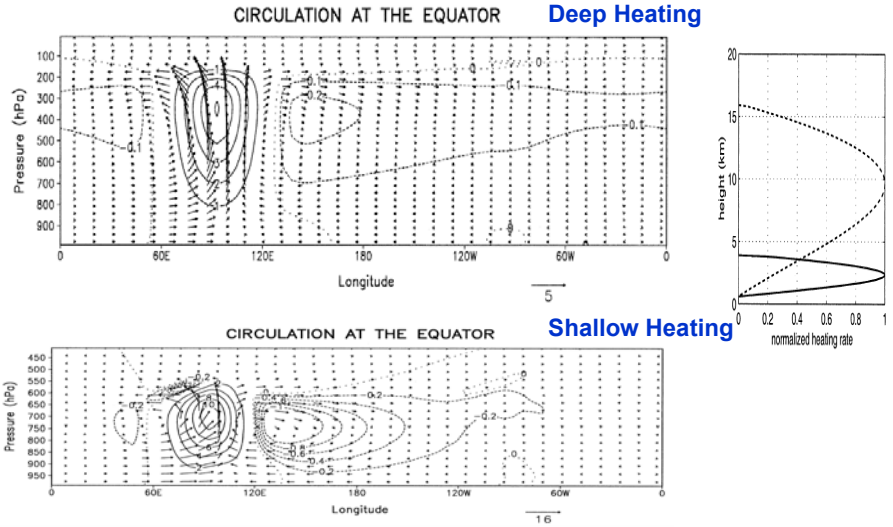

Shallow (congestus) heating is more effective than deep heating for the low-level moisture convergence (Wu 2003)

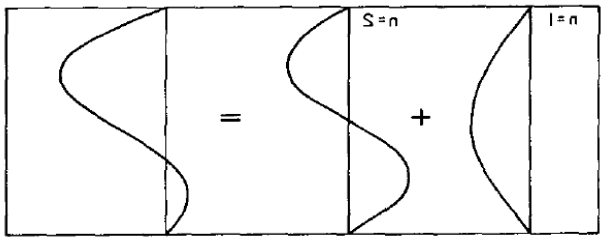

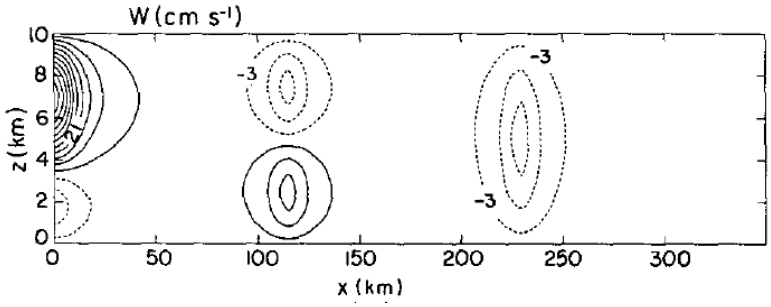

(Nicholls et al. 1991b)

環境場に与える効果
2. 大気層のOVER TURNING

Simulation

応答問題

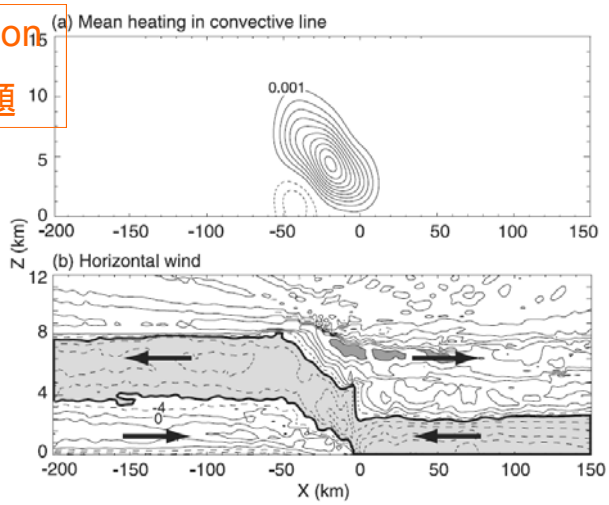

Convective line 域の非断熱加熱を2hr平均

↓

Forcing として与えた

重力波応答として3kmの厚さのインフローが対流域に入って上昇し、中上層で出て行く流れが再現された。

Figure 7. Two-dimensional model simulation results for a leading-line/trailing-stratiform squall line mesoscale convective system (MCS). (a) Time mean thermal forcing meant to represent the forcing from the leading convective line alone. Contour interval is 0.001 K s^{-1}. (b) Horizontal velocity at time t = 6 hours generated by the thermal forcing in Figure 7a. Horizontal velocity contours are at intervals of 4 m s^{-1}. Arrows indicate direction of the horizontal flow. Cold pool forward boundary is at x = 0. Bold contour and shading emphasize layer inflow constituting the layer ascent of air originating ahead of the storm and rising through it. Adapted from *Pandya and Durran* [1996].

(Pandya and Durran 1996)

Simulation

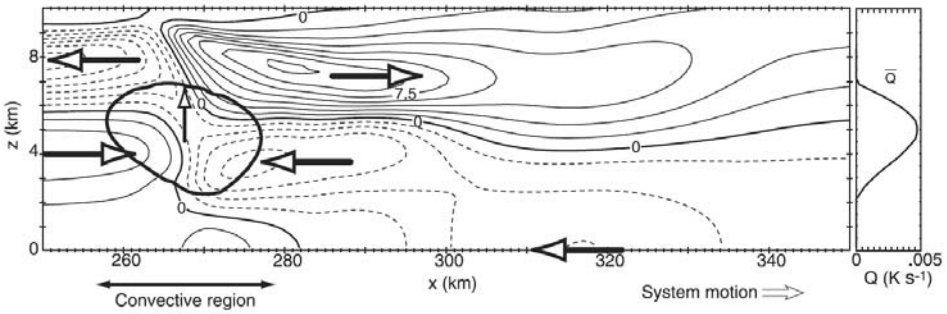

Figure 8. Response to convective region heating in a simulated MCS. The circle outlined by the bold line shows the area in which heating was applied. Contours show the horizontal velocity response to the mean convective region heating profile indicated in the right-hand panel. Contours of perturbation horizontal wind in the plane of the cross section are at intervals of 1.5 m s^{-1}, with dashed contours indicating right-to-left flow in the cross section. Large arrows emphasize direction of motion. Adapted from *Fovell* [2002].

インフローの厚さがやや厚い(3-6km)が、
ほぼPandya and Durran 1996と同じ結果

(Fovell 2002)

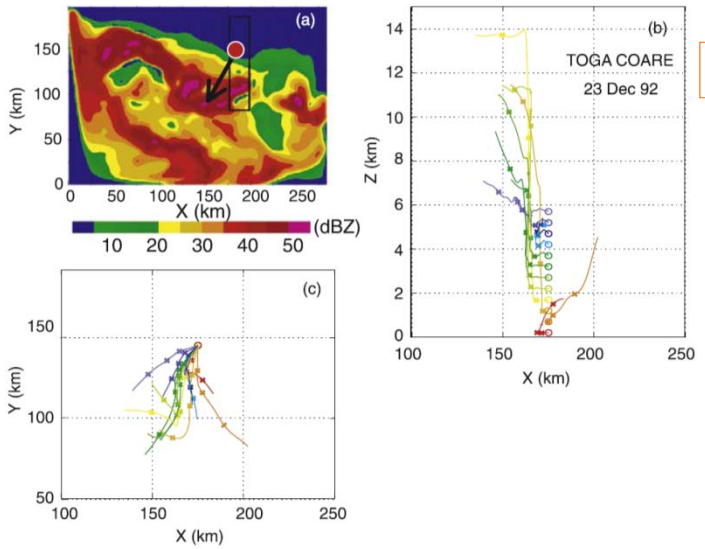

Simulation

Figure 12. (a) Model-simulated reflectivity (dBZ) for an MCS over the western tropical Pacific. The box in Figure 12a indicates the horizontal span of the initial tracer distribution used in trajectory calculations. Twelve trajectories were calculated over 3.5 hours of model time. Initial tracer locations are located 500 m apart in a vertical column. Initial location is marked by the small circle. Arrow indicates general direction of low level flow. (b) Projection of the trajectory paths onto the *x-z* (west-east) vertical plane and (c) projection onto the *x-y* (horizontal) plane. Origins are indicated by circles; hourly positions are shown by crosses. Adapted from *Mechem et al.* [2002].

(Mechem et al. 2002)

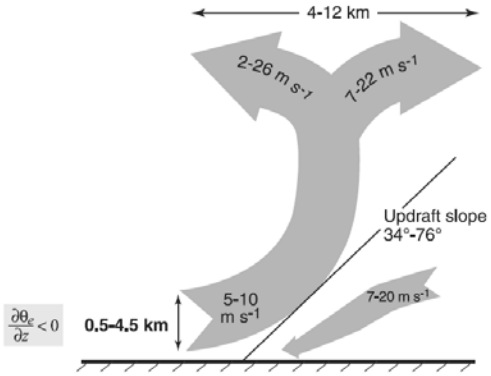

Airborne Doppler Radar

Figure 9. Schematic of airflow in the convective regions of an MCS over the western tropical Pacific as observed by airborne Doppler radar in Tropical Ocean–Global Atmosphere Coupled Ocean-Atmosphere Response Experiment (TOGA COARE). The numbers (from bottom to top) indicate the observed ranges of values of the depth of the inflow layer, horizontal relative velocity of inflow and outflow air currents, the slope of the updraft (angle measured relative to the ocean surface), and the width of the divergent region aloft. The horizontal directional differences of the low level updraft inflow and middle level downdraft inflow were often significantly different from 180°. Based on figures and tables from *Kingsmill and Houze* [1999a].

TOGA COARE

33 dual-Doppler Radar analyses from 25 different MCS + countless single Doppler sweeps from vertically scanning Doppler radars

- 上昇域はほとんど必ず傾斜した層状の上昇であり、明らかにダウンドラフトから形成されたcold poolの上に乗り上げる流れであった。
- 傾斜した上昇流の層の厚さは、0.5-4.5kmの範囲であり、大気境界層より明白に厚かった。

(Kingsmill and Houze 1999)

環境場に与える効果
3. 運動量輸送

背景　　CMT（対流による運動量輸送）について

背景東西風 $\bar{u}$ の tendency

$$\frac{\partial \bar{u}}{\partial t} = \boxed{-\frac{1}{\bar{\rho}}\left(\frac{\partial \bar{\rho}\,\overline{uu}}{\partial x} + \frac{\partial \bar{\rho}\,\overline{uv}}{\partial y} + \frac{\partial \bar{\rho}\,\overline{uw}}{\partial z}\right)} - \frac{1}{\bar{\rho}}\frac{\partial \bar{p}}{\partial x} + f\bar{v} + \bar{F}$$

u, v, w を（ $u = \bar{u} + u'$ ） のように背景場と擾乱項に置き換えて移流項を整理

$$(\text{移流項}) = -\frac{1}{\bar{\rho}}\left(\frac{\partial \bar{\rho}\,\bar{u}\,\bar{u}}{\partial x} + \frac{\partial \bar{\rho}\,\bar{u}\,\bar{v}}{\partial y} + \frac{\partial \bar{\rho}\,\bar{u}\,\bar{w}}{\partial z} + \frac{\partial \bar{\rho}\,\overline{u'u'}}{\partial x} + \frac{\partial \bar{\rho}\,\overline{u'v'}}{\partial y} + \boxed{\frac{\partial \bar{\rho}\,\overline{u'w'}}{\partial z}}\right)$$

青：背景場による移流　　茶：水平の擾乱項の相関の効果　・・・通常小さい
(Arakawa and Shubert 1974, Wu 1994)

赤：水平と鉛直の擾乱項の相関による効果　≒　CMTの効果

Miyakawa 2010, 学位論文

背景

CMT（対流による運動量輸送）の要点

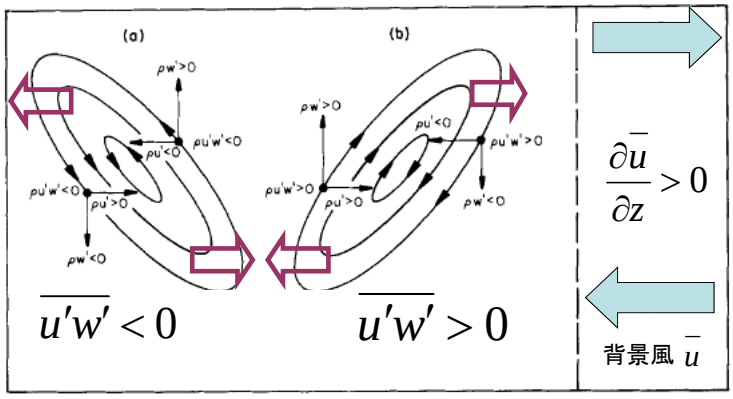

(Moncrieff ,1992)

$-\frac{1}{\bar{\rho}}\left(\frac{\partial \bar{\rho}\,\overline{u'w'}}{\partial z}\right)$ は背景場の水平風 $\bar{u}$ の時間変化に寄与する。

$\overline{u'w'}\frac{\partial \bar{u}}{\partial z} > 0$ の場合、運動量輸送が水平風の鉛直シアを強める方向に働く。

→ up gradient

Miyakawa 2010, 学位論文

LeMone 1983

Momentum Transport by a Line of Cumulonimbus

MARGARET A. LEMONE

National Center for Atmospheric Research,[1] Boulder, CO 80307

(Manuscript received 9 November 1982, in final form 7 March 1983)

ABSTRACT

The vertical transport of horizontal momentum normal to a line of cumulonimbus observed during GATE on 14 September 1974 is against the vertical momentum gradient, contrary to the predictions of mixing-length theory. Data from repeated aircraft passes normal to the line's axis at heights from 0.15 to 5.5 km are used to document the flux and determine its source. The flux is concentrated in roughly a 25 km wide "active zone" just behind the leading edge of the line, in kilometer-scale convective updrafts accelerated upward by buoyancy and toward the rear of the line by mesoscale pressure forces. The fall in mesoscale pressure from the leading edge to the rear of the active zone is mainly hydrostatic, resulting from relatively high virtual temperatures and the 60 degree tilt of the leading edge from the vertical, with the clouds at the surface well ahead of those aloft.

Evaluation of the terms in the momentum-flux generation equation confirms that the above process, reflected by the velocity–buoyancy correlation term, is responsible for generating momentum flux of the observed sign. The component of momentum flux parallel to the axis of the convective band is generated much like "down-gradient" momentum flux within the fair-weather subcloud layer.

Momentum Budget of a Squall Line with Trailing Stratiform Precipitation: Calculations with a High-Resolution Numerical Model

MING-JEN YANG* AND ROBERT A. HOUZE JR.

Department of Atmospheric Sciences, University of Washington, Seattle, Washington

(Manuscript received 3 July 1995, in final form 20 June 1996)

ABSTRACT

In this paper, the authors investigate the momentum budget of a squall line with trailing stratiform precipitation by examining how the momentum balance varies with respect to the storm's internal structure. In particular, the authors determine differences between the momentum budgets of the convective and stratiform precipitation regions, which are physically distinct parts of the storm. The results from a high-resolution nonhydrostatic numerical simulation of the two-dimensional segment of the 10–11 June 1985 PRE-STORM squall line are used. The momentum equation is averaged over a 300-km-wide large-scale area for time periods of 1 h. On the 1-h timescale, the convective-scale temporal variations of horizontal and vertical velocities are nearly uncorrelated, and thus their contribution to the momentum flux is negligible. The remaining standing-eddy and mean-flow circulations account for the momentum flux on this timescale. The combination of the standing eddy and mean flow behave almost exactly like Moncrieff's idealization of two-dimensional steady-state squall line flow.

Because the standing-eddy circulation and the pressure-gradient acceleration vary from one part of the storm to another, the interplay of forces leading to the large-scale momentum tendency also differs strongly from one subregion to another. The convective precipitation region dominates the momentum budget at low levels, where the standing-eddy flux convergence produces a forward acceleration that slightly outweighs the rearward pressure-gradient acceleration. At midlevels, both the convective and stratiform precipitation regions contribute to the net large-scale momentum tendency. The pressure-gradient forces in the convective and stratiform precipitation regions are both strong but oppositely directed; however, the rearward standing-eddy flux convergence in the convective precipitation region is also strong; thus, the net large-scale momentum tendency at midlevels is rearward. At upper levels, the momentum budget is completely dominated by the stratiform precipitation region, where a strong forward-directed pressure-gradient acceleration dominates the net large-scale momentum tendency.

These differences between the momentum budgets of the convective and stratiform precipitation regions suggest that rather different large-scale momentum tendencies can arise as a function of storm structure; storms with strong convective precipitation regions and weak stratiform precipitation regions would produce momentum tendencies quite different from storms with well-developed stratiform precipitation regions.

スコールライン型のMCSの運動量収支

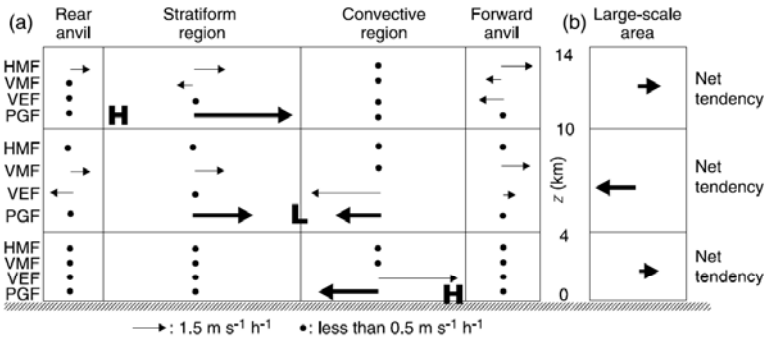

Figure 43. (a) A block diagram showing the balance of area-weighted momentum budget terms over four subregions of a squall line MCS. Rightward (leftward) arrows are for rear-to-front (front-to-rear) momentum tendency for individual terms in the cross-line momentum budget equation (HMF, horizontal mean flux, VMF, vertical mean flux, VEF, vertical eddy flux, and PGF, pressure gradient force). The length of the arrow is proportional to the layer-averaged tendency produced by each budget term. A dot is for the tendency <0.5 m s^{-1} h^{-1}. H and L indicate approximate locations of centers of mesoscale high- and low-pressure perturbations, respectively. (b) Same as in Figure 43a except for net momentum tendency. Adapted from *Yang and Houze* [1996].

References (12/08-09/2005)

Text Books
• R. A. Houze Jr., 1993: Cloud Dynamics, Academic Press, pp. 573

Papers
• Biggerstaff, M. I., and and R. A. Houze, Jr., 1991: Kinematics and precipitation structure of the 10-11 June 1985 squall line, Mon. Wea. Rev., 119, 3035-3065.
• Biggerstaff, M. I., and and R. A. Houze, Jr., 1993: Kinematics and microphysics of the transition zone of a midlatitude squall-line system, J. Atmos. Sci.
• Churchill, D. D., and R. A. Houze, Jr., 1984: Development and structure of winter monsoon cloud clusters on 10 December 1978, J. Atmos. Sci., 41, 933-960.
• Chen S. S. and W. M. Frank. 1993: A Numerical Study of the Genesis of Extratropical Convective Mesovortices. Part I: Evolution and Dynamics. J. Atmos. Sci.: 50, 2401–2426.
• Cheng, C.-P., and R. A. Houze, Jr., 1979: Sensitivity of diagnosed convective fluxes to model assumptions, J. Atmos. Sci., 37, 774-783.
• Fovell, R. G., and Y. Ogura, 1988: Numerical simulation of a midlatitude squall line in two dimensions. J. Atmos. Sci., 49, 1427-1442.
• Fovell, 2002: Upsteam influence of numerically simulated squall line storms. Quart. J. Roy. Met. Soc., 128, 893-912.
• Frank, 1978
• Gamache, J. F. and R. A. Houze, Jr., 1985: Further analsysis of the composite wind and thermodynamic structure of the 12 September GATE squall line., Mon. Wea. Rev., 113, 1241-1259.
• Gray, W. M., 1998: The formation of tropical cyclones. Meteorol. Atmos. Phys. 67, 37-69.
• R. A. Houze, Jr., 1977: Structure and dynamics of a tropical squall-line system. Mon. Wea. Rev., 105, 1540-1567.

• R. A. Houze, Jr. et al. 1989: Interpretation of doppler-weather-radar displays in midlatitude mesoscale convective systems. Bull. Amer. Meteor. Soc., 70, 608-619.
• R. A. Houze, Jr., 1989: Observed structures of mesoscale convective systems and implications for large-scale heating. Quart. J. Roy. Met. Soc., 115, 425-461.
• R. A. Houze, Jr., 2004: Mesoscale Convective Systems, Reviews of Geophysics, 42, RG4003/2004, paper number 2004RG000150
• R. A. Houze, Jr., and C.-P. Cheng, 1977: Radar characteristics of tropical convection observed during GATE: Mean properties and trends over the summer monsoon. Mon. Wea. Rev., 105, 964-980.
• Johnson, R. H., and P. J. Hamilton, 1988: The relationship of surface pressure features to the precipitation and airflow structure of an intense midlatitude squall line. Mon. Wea. Rev., 116, 1444-1472.
• Kingsmill, D. E., and R. A. Houze Jr., 1999: Kinematic characteristics of air flowing into and out of precipitating convection over the west Pacific wram pool: An airborne Doppler radar survey, Q. J. R. Meteorol. Soc., 125, 1165-1207.
• Leary, C. A. and Houze, R. A., Jr., 1979: The structure and evolution of convection in a tropical cloud cluster. J. Atmos. Sci., 36, 437-457.
• Leary, C. A. and Houze, R. A., Jr., 1979: Melting and evaporation of hydrometeors in precipitation from the anvil clouds of deep tropical convection, J. Atmos. Sci., 36, 669-678.
• LeMone et al. 1984:
• Maddox, R. A., 1980: A satellite-based study of midlatitude mesoscale convective complexes. Peprints, Eighth Conference on Weather Forecasting and Analysis, Denver, CO, American Meteorological Society, Boston, 329-338.
• Miyakawa, T., Y. N. Takayabu, T. Nasuno, H. Miura, M. Satoh, and M. W. Moncrieff, (2012), Convective momentum transport by rainbands within a Madden-Julian oscillation in a global nonhydrostatic model with …..J. Atmos. Sci., in press
• Moncrieff, M. W., 1992: Organized convective systems: Archetypal dynamical models, mass and momentum flux theory, and parameterization, Q. J. R. Meteorol. Soc., 107, 29-50.

• Nicholls, M. E., R. A. Pielke, and W. R. Cotton, 1991: Thermally forced gravity waves in an atmosphere at rest, J. Atmos. Sci., 48, 1869-1884
• Pandya, R. and D. Durran, 1996: The influence of convectively generated thermal forcing on the mesoscale circulation around squall lines, J. Atmos. Sci. 53, 2924-2951.
• Roux 1988:
• Schumacher, C, and R. A. Houze Jr., 2003: Stratiform rain in the tropics as seen by the TRMM precipitation radar. J. Climate, 16, 1739-1756.
• Schumacher, C, R. A. Houze Jr., and I. Kraucunas, 2004: The tropical dynamical response to latent heating estimates derived from the TRMM Precipitation Radar, J. Atmos. Sci., 61, 1341-1358.
• Sun, J., and F. Roux, 1988: Thermodynamic structure of the trailing-stratiform regions of two west African squall lines, Ann. Geophysicae, 6, 659-670.
• Tao, W.-K., and J. Simpson, 1989: Modeling study of a tropical squall-type convective line. J. Atmos. Sci., 46, 177-202.
• Velasc, I., and J. M. Fritsh, 1987: Mesoscale convective complexes in the Americas, J. Geophys. Res. 92, 9591-9613.
• Williams, M., and Houze, R. A., Jr., 1987: Satellite-observed characteristics of winter monsoon cloud clusters. Mon. Wea. Rev., 115, 505-519.
• Yang, M.-J., and R. A. Houze, 1996: Momentum budget of a squall line with trailing stratiform precipitation: calculations with a high-resolution numerical model. 53, 3629-3651.
• Zher 1992:
• Zipser, E. J., 1977: Mesoscale and convective-scale downdrafts as distinct components of squall-line circulation. Mon. Wea. Rev., 105, 1568-1589.
• Zipser, E. J., R. J. Meitin, and M. A. LeMone, 1981: Mesoscale motion fields associated with a slowly moving GATE convective band, J. Atmos. Sci., 38, 1725-1748.